

Article

In Situ Modification of $\text{CaF}_2\text{-SiO}_2\text{-Al}_2\text{O}_3\text{-MgO}$ Flux Applied in the Aluminium-Assisted Transfer of Titanium in the Submerged Arc Welding of Carbon Steel: Process Mineralogy and Thermochemical Analysis

Theresa Coetsee *  and Frederik De Bruin

Department of Materials Science and Metallurgical Engineering, University of Pretoria, Pretoria 0002, South Africa; fjdb.1953@gmail.com

* Correspondence: theresa.coetsee@up.ac.za

Abstract: Flux formulations are specified to target chemical and physico-chemical parameters. Chemical parameters set flux element transfer behaviours and weld metal oxygen contents. Physico-chemical parameters such as slag viscosity, surface tension and melting range are targeted to ensure an acceptable weld bead profile and surface appearance. Slag detachability is an important physico-chemical property required to ensure high welding productivity, smooth weld bead surface and no slag entrapment. Here, bead-on-plate welding tests were made with and without metal powder additions, including aluminium powder as a de-oxidiser. Difficult slag detachability was observed in weld runs made with metal powder additions. Mineralogy of the post-weld slags, and thermochemical calculations, show that the flux was modified due to the aluminothermic reduction of MnO and SiO_2 from the slag to form alumina. Increased quantities of spinel phase were identified in the post-weld slag samples, at the weld pool–slag interface. The combined effect of increased slag viscosity, from increased spinel in the slag, and lowered weld pool solidus temperature, resulted in the formation of a rough bead surface morphology, which, in turn, caused mechanical fixation of the slag to the weld bead. Flux modification to higher CaF_2 content should ensure that higher quantities of spinel phase can be tolerated in the slag.

Keywords: slag; flux; phase chemistry; fluoride; spinel; mineralogy; oxy-fluoride; glass



Citation: Coetsee, T.; De Bruin, F. In Situ Modification of $\text{CaF}_2\text{-SiO}_2\text{-Al}_2\text{O}_3\text{-MgO}$ Flux Applied in the Aluminium-Assisted Transfer of Titanium in the Submerged Arc Welding of Carbon Steel: Process Mineralogy and Thermochemical Analysis. *Minerals* **2022**, *12*, 604. <https://doi.org/10.3390/min12050604>

Academic Editor: Mark I. Pownceby

Received: 26 April 2022

Accepted: 9 May 2022

Published: 11 May 2022

Publisher's Note: MDPI stays neutral with regard to jurisdictional claims in published maps and institutional affiliations.



Copyright: © 2022 by the authors. Licensee MDPI, Basel, Switzerland. This article is an open access article distributed under the terms and conditions of the Creative Commons Attribution (CC BY) license (<https://creativecommons.org/licenses/by/4.0/>).

1. Introduction

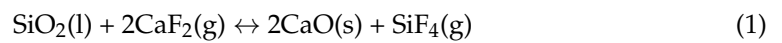
Submerged arc welding (SAW) consists of complex interactions of physical, electrical and chemical effects in the arc cavity [1,2]. In addition to the machine input selections of current, weld wire diameter, voltage, travel speed, current polarity and electrode (weld wire) extension, the flux chemistry and its chemical effects on the molten flux (slag) are important process input selections [3,4]. The welding flux performs several process functions: it forms a slag (molten flux) layer around the arc plasma to shield the arc from atmospheric oxygen and nitrogen, it limits weld metal hydrogen absorption from moisture, it limits arc energy losses from the arc to the environment by forming an opaque low conductivity slag boundary around the arc cavity, and it transfers alloying elements to the weld metal [3,4]. In carbon steel SAW, the weld pool manganese and silicon contents are controlled via flux formulation, in combination with the weld wire and base metal chemistries [3–5]. Micro-alloying may also be performed via the molten flux; for example, the addition of Ti to the weld pool [3,4]. Significant quantities of fluoride minerals, typically CaF_2 , are added to the flux to ensure that the flux melts at approximately 50 °C lower than the weld metal [6]. For carbon steel, this translates to a relatively low flux melting temperature, as the steel solidus temperature is in the order of 1480 °C; therefore, the flux should be sufficiently molten at approximately 1400 °C. This temperature guideline appears

to be selected to ensure that the slag solidifies after the weld pool steel has solidified [6]. The maximum weld pool temperature has been reported as 2000 °C [7,8]. Due to this wide temperature range applied to the slag in SAW, the slag properties also change widely across this temperature range. The flux is also formulated to be a “short” or “long” slag, depending on the welding application [9,10]. Most fused fluxes form “short” slags since their compositions are selected close to the multi-component system’s eutectic composition [10]. Consequently, the difference in the slag liquidus temperature and solidus temperature is small and the slag transitions over a small temperature interval from fluid to viscous [9–11]. Most agglomerated fluxes form “long” slags with the opposite melt characteristics to a “short” slag [11]. In addition to its role in setting the liquidus and solidus temperatures in the slag, CaF₂ is also used to set the process physico-chemical properties of the slag to enhance its process application. For example, the slag viscosity and surface tension are also influenced by CaF₂ as the F[−] serves as network modifier anion [12]. Several recent studies are available on SAW flux development, linking physico-chemical properties of the molten flux(slag) to flux input compositions via regression studies and fundamental slag structure studies, respectively [13,14]. However, these studies were not focused on the multi-component system of CaF₂-SiO₂-Al₂O₃-MgO, relevant to this study. Furthermore, even though fluoride-based fluxes are used in the continuous casting of steel and electro slag refining (ESR), the target compositions in these types of fluxes differ substantially from the flux composition ranges as applied in SAW with either much lower or much higher CaF₂ content and high CaO contents [15,16].

Another critical physical parameter is slag detachability from the weld metal. Good slag detachability is required to ensure high welding productivity because no extra time should be used to mechanically remove any slag sticking to the weld metal. Additionally, in multi-pass welding, an easily detachable slag is critical to prevent any contamination of subsequent weld runs due to remnant slag added into the weld pool [17]. Fundamental reasons given for good slag detachability vary from ensuring a large difference in thermal expansion between the solid slag and weld metal; to preventing the formation of excessive quantities of high-melting-point phases such as spinel (MgO·Al₂O₃), Cr₂O₃ or perovskite (CaTiO₃); to the prevention of formation of a chemical bond via interlayer formation between the slag and weld metal; and to ensuring that a low-strength slag is formed from the molten flux [3,7,17–20]. Conflicting findings have been reported; for example, in one study, perovskite in the slag was found to be detrimental to slag detachability [20], and in another, perovskite was recommended to aid in slag detachability due to its higher coefficient of thermal expansion, as compared with the underlying high Ni–Cr alloy weld metal [21]. In some instances, a small quantity of solid phase is added to improve slag detachability. For example, up to 2 mass% ZrO₂ is added to basic fluxes to compensate for their similar thermal expansion coefficient to that of the steel weld metal [3]. Spinel can also be used to induce micro-stresses in the glass phase to enhance slag detachability due to its different thermal expansion coefficient to the solidified glass phase [9]. It is well stated that the application of the weld flux in the particular welding set-up must be investigated in the welding tests to make any conclusions on slag detachability because the interaction of chemical and welding parameters in the process determines slag detachability [18].

The addition of CaF₂ in the flux formulation is also used to control the weld metal ppm O and limit hydrogen pick-up into the weld metal. Although the weld pool and arc cavity are isolated from the atmosphere, oxygen is added into the weld pool via the dissociation of oxides in the flux. Oxides decompose in the arc plasma due to high temperatures, in the order of 2000 °C to 2500 °C [22,23]. Oxygen is adsorbed onto molten weld wire droplets in the arc plasma and transferred into the weld pool via the molten wire droplets [24,25]. The rank of oxide stability in the arc plasma was measured from least stable to most stable as MnO and SiO₂, MgO, Al₂O₃, TiO₂, Na₂O, K₂O, and CaO [24]. The effect of fluorides in the flux is to lower the P_{O₂} in the arc cavity by forming fluorine-based compounds via reactions similar to reaction (1) between SiO₂ and CaF₂ [26,27]. Similarly, the P_{H₂} is lowered to limit hydrogen pick-up into the weld metal [28,29]. Hydrogen pick-up in the weld pool

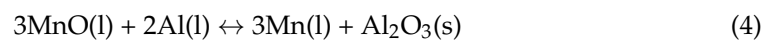
is also limited by reactions of water vapour and CaF_2 , according to reaction (2), and by formulating the flux chemistry for increased hydrogen dissolution capacity [27–29].



The empirically determined trend of flux basicity (BI) vs. ppm O in the weld metal is generally used to design fluxes for the target oxygen content in the weld metal. The BI expression is shown in Equation (3) in mass% values [30].

$$\text{BI} = [\text{CaF}_2 + \text{CaO} + \text{MgO} + \text{BaO} + \text{SrO} + \text{Na}_2\text{O} + \text{K}_2\text{O} + \text{Li}_2\text{O} + 0.5(\text{MnO} + \text{FeO})]/[\text{SiO}_2 + 0.5(\text{Al}_2\text{O}_3 + \text{TiO}_2 + \text{ZrO}_2)] \quad (3)$$

By ensuring that the flux solidus temperature is lower than the weld pool steel solidus temperature, maximum time is allowed for chemical interaction between the flux and the underlying weld pool steel. Increased reaction time between the weld pool steel and covering slag is important to ensure that oxide inclusions have more time to float out of the weld pool steel, to the slag–weld pool interface to ensure clean steel in the weld metal [31]. The flux chemical composition is usually not changed significantly during slag formation in SAW, although some FeO is added due to the oxidation of steel Fe to FeO [22,32–35]. In our recent studies, aluminium powder was applied in the SAW process as a de-oxidiser element to increase metal powder alloying in the weld pool [36–39]. The added aluminium powder significantly changed the flux chemistry via reduction reactions of oxides of SiO_2 and MnO, similar to reaction (4) for MnO reduction by aluminium. The increased Al_2O_3 content in the slag has important effects on the physico-chemical properties of the slag.



The objective of this study was to investigate slag phase chemistry modifications due to the application of aluminium powder in the alloying of carbon steel weld metal and use this information to interpret slag detachability differences. The post-weld slag chemistry is discussed with the aid of calculations in FactSage 7.3 thermochemical software, using the FToxid database [40,41].

2. Materials and Methods

SAW welding tests were made as bead-on-plate runs onto steel plates of 350 mm in length, 12 mm plate thickness and 300 mm plate width. Weld heat input was 2.0 kJ/mm (500 A, 28 V, 42 cm/min) welded DCEP (direct current electrode-positive) with a 3.2 mm diameter wire. Structural steel grade EN 10025-2 was used as a base plate material. The chemical analyses of the base plate and weld wire are summarised in Table 1. Major element levels in the weld wire analysis are from the supplier's specification sheet, supplied by Afrox Ltd., Johannesburg, South Africa. The base plate steel was analysed by optical emission spectroscopy (OES), model SpectroMax XF, 2018, from SPECTRO Analytical Instruments GmbH, Kleve, Germany. The oxygen content in the base plate and weld wire was analysed by combustion method.

Table 1. Composition of steel base plate and weld wire used in welding tests.

Sample	%C	%Si	%Mn	* O	%Al	%P	%S	%Ti	%Cu	%Cr	Balance
Plate	0.120	0.155	1.340	7	0.067	0.019	0.007	0.005	0.030	0.160	Fe
Wire	0.110	0.137	0.990	3	0	0.009	0.023	0	0.140	0	Fe

* ppm.

Commercial agglomerated flux of the composition presented in Table 2 was used in the welding experiments, following a previous detailed study on a selection of commercial

agglomerated fluxes [42]. This is an aluminate basic flux (basicity index (BI) = 1.4) and was extensively analysed as reported previously [42]. The main consideration in the selection of this flux is its likely thermodynamic stability in the presence of aluminium powder as a de-oxidiser element. The metal powder additions used as additions in the SAW tests were sourced as Al (99.7% Al) supplied by Sigma-Aldrich, St. Louis, MO, USA, Ti (99.5% Ti) supplied by PLS Technik GmbH & Co., Niedernberg, Germany, and Cu (99.8% Cu) supplied by Goodfellow, Hintingdon, UK.

Table 2. Bulk chemistry of flux used in welding tests (mass%).

%MnO	%CaO	%SiO ₂	%Al ₂ O ₃	%CaF ₂	%MgO	%FeO	%TiO ₂	%Na ₂ O	%K ₂ O
6.8	0.1	19.6	24.9	17.9	22.2	2.4	1.0	1.6	0.2

The welded plate was sectioned to remove cross-section samples of the weld metal for major element analyses by OES, and total oxygen content analyses were performed by the combustion method. Due to higher concentrations of Ti and Al in the weld metal, compared with low-carbon steel, the %Al and %Ti were analysed by ICP-OES (inductively coupled plasma optical emission spectrometry). The weld metal sample was digested by a three-acid digestion method, using HNO₃, HCl and HF. The weld metal results confirmed significant alloying of the weld metal from the added metal powders, and also increased %Mn and %Si in the weld metal due to the aluminothermic reduction of MnO and SiO₂ from the flux [36,38]. Due to significant changes measured in the bulk compositions of post-weld slags, compared with the original flux chemistry, these changes are quantified and interpreted in this study. Furthermore, slag removal from MP1 and MP3 welds, made with metal powder additions were difficult, requiring light mechanical impact. In comparison, the slag from the BC weld, welded in the absence of metal powder additions, effectively self-removed without the requirement of any mechanical impact.

The post-weld slag bulk chemistry and mineralogy were analysed. Slag bulk chemistry was analysed by inductively coupled plasma optical emission spectrometry (ICP-OES). Sample digestion in HCl and HF was used for major element analysis, and sample fusion in Na₂O₂ and Na₂CO₃, with subsequent digestion in HCl was used for minor element analysis. The slag F-content was analysed by the titration method, following sample digestion in HClO₄. Slag crystallinity was analysed by XRD (X-ray diffraction) analyses. The XRD samples were prepared according to the standardised Panalytical backloading system, which provides a nearly random distribution of the particles. The samples were analysed using a PANalytical X'Pert Pro powder diffractometer (Malvern Panalytical, Almelo, The Netherlands) in θ - θ configuration with an X'Celerator detector and variable divergence and fixed receiving slits with Fe-filtered Co-K α radiation ($\lambda = 1.789 \text{ \AA}$). The mineralogy was determined by selecting the best-fitting pattern from the ICSD database to the measured diffraction pattern, using X'Pert Highscore plus software (version 4.9).

Phase chemistry of the slag phases in the sample polished sections were assessed by SEM (scanning electron microscopy). Phase chemistry analysis was measured by using a Zeiss crossbeam 540 FEG (field emission gun) scanning electron microscope. EDX (energy dispersive X-ray) analyses were performed at 20 kV and 5.6 mm working distance. The SEM analyses were performed at the edge of the slag surface which was in contact with the weld metal during welding. Therefore, comparison of the slag SEM analyses at this interface to the bulk slag chemistry should show up any major composition differences that occurred due to the welding process.

3. Results

The post-weld slag bulk chemistry in Table 3 illustrates significant chemistry changes in the MP1 and MP3 slags when compared with the Base Case (BC) slag. These changes are due to the addition of metal powder to the weld pool, as compared with the Base Case (BC) slag formed in the absence of metal powder additions [36–39]. Mainly, MnO and SiO₂

decreased and Al_2O_3 and TiO_2 increased, as shown in the Table 3 analyses for MP1 and MP3, relative to the BC slag analysis. The increase in Al_2O_3 is due to the use of aluminium metal powder as a de-oxidiser metal in the weld pool, and due to the aluminothermic reduction of MnO and SiO_2 [36,38]. The increased TiO_2 content is due to the oxidation of Ti to its oxide. Although some Cu was analysed in the MP3 bulk slag, the presence of copper in the slag SEM phase analysis was not confirmed. Therefore, the Cu analysed in the bulk slag chemistry was most likely due to metallic Cu loss to the slag.

Table 3. Bulk chemical compositions of post-weld slags (mass%).

Sample	%MnO	%CaO	%SiO ₂	%Al ₂ O ₃	%CaF ₂	%MgO	%FeO	%TiO ₂	%Na ₂ O	%K ₂ O
BC	6.5	2.3	19.8	25.9	14.3	23.3	4.4	1.0	2.2	0.2
MP1	4.6	3.4	15.1	31.6	11.0	23.2	4.0	5.4	1.6	0.2
MP3	3.8	2.6	11.7	34.8	8.6	18.3	4.4	14.4	1.3	0.2

Figure 1 illustrates that the XRD analyses identified similar crystalline phases in all the post-weld slags, namely, spinel (MgAl_2O_4), corundum (Al_2O_3), fluorite (CaF_2), periclase (MgO), quartz (SiO_2) and the $\text{NaMg}_3\text{AlSi}_3\text{O}_{10}\text{F}_2$ oxy-fluoride phase. The characteristic hump in the count rate values at low 2θ values indicates the presence of amorphous phase. Figures 2–6 display the typical phase assembly in BSE (backscattered electron) images in each post-weld slag sample, and the associated phase compositions analysed by SEM. Although the BC slag sample was previously investigated in detail, a new area of analysis is shown in Figure 2 to show the unaltered molten flux for comparison with the altered slags from the MP1 and MP3 tests shown in Figures 3–6 [42].

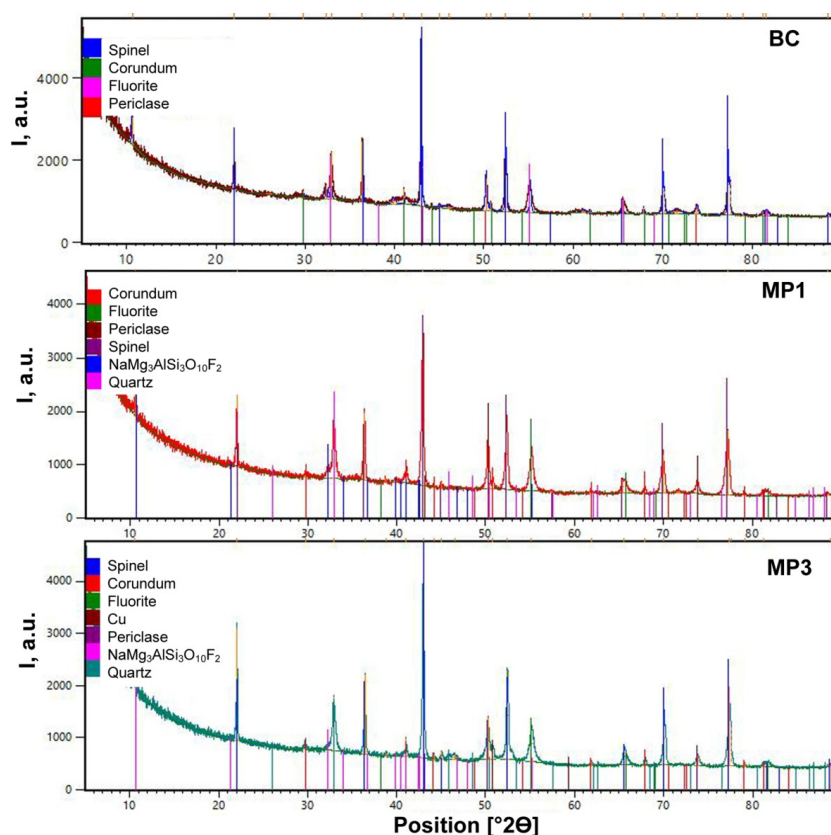


Figure 1. Analysed XRD patterns of post-weld slags in Table 3.

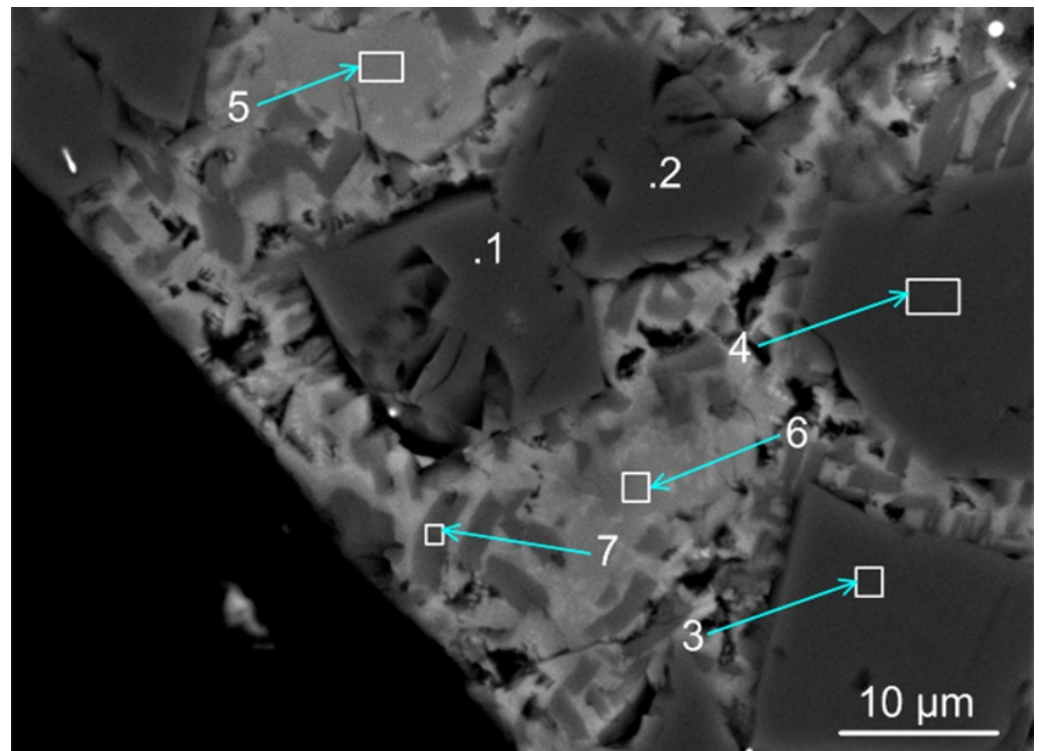


Figure 2. BSE image of the slag area at the slag–weld metal interface: BC slag sample. (See Table 4 for the analyses of the numbered phases in Figure 2).

Table 4. SEM analyses of marked phase positions in Figure 2 (mass%).

Position	%Al	%Mg	%Ca	%F	%Si	%Ti	%Mn	%Fe	%Na	%K	%O	Phase
1	35.1	15.9	0	0	0	0.3	2.3	0	0	0	46.4	Spinel
2	35.1	15.8	0.1	0	0	0.3	2.2	0.3	0	0	46.2	Spinel
3	35.1	15.9	0	0	0	0.4	2.2	0.3	0	0	46.0	Spinel
4	35.1	16.0	0	0	0	0.4	2.3	0.4	0	0	45.8	Spinel
5	4.2	11.3	14.6	10.5	13.9	0.6	6.0	0.5	2.9	0	35.5	Glass
6	3.3	13.9	13.3	11.4	13.9	0.6	6.0	0.3	2.4	0	34.8	Glass
7	7.4	16.2	7.0	10.9	14.7	0.8	2.5	0	2.4	0.7	36.9	Glass
Bulk Slag	13.7	14.1	9.0	7.0	9.2	0.6	5.0	3.4	1.6	0.2	36.1	

The presence of spinel crystals in the Al–Mg–Ca–F–Si–Ti–Mn–Fe–K–Na–O oxy-fluoride matrix glass is confirmed in the analyses summarised in Table 4, for the marked phase areas in Figure 2. The spinel crystals are close to 20 μm in cross-sectional dimension. Feathery wisps appear in the matrix glass, such as in position 7 in Figure 2.

Figure 3 shows a BSE image of an area in the MP1 slag. The phase areas consist of Ti-containing spinel crystals in the oxy-fluoride glass matrix phase. The presence of a large cluster of spinel crystals at the top left-hand edge of the sample is clear, as seen from the octahedral crystalline shape of the spinel crystals. The analyses in Table 5 confirm the pick-up of Ti in the spinel and matrix glass phases, compared with the BC phase analyses in Table 4. Some variability is seen in the glass phase fluoride content in Table 5. Some variability in the fluoride contents in similar samples was reported for the phase area analyses in agglomerated flux material of the MgO–Al₂O₃–SiO₂–CaF₂ system, melted under laboratory conditions [43].

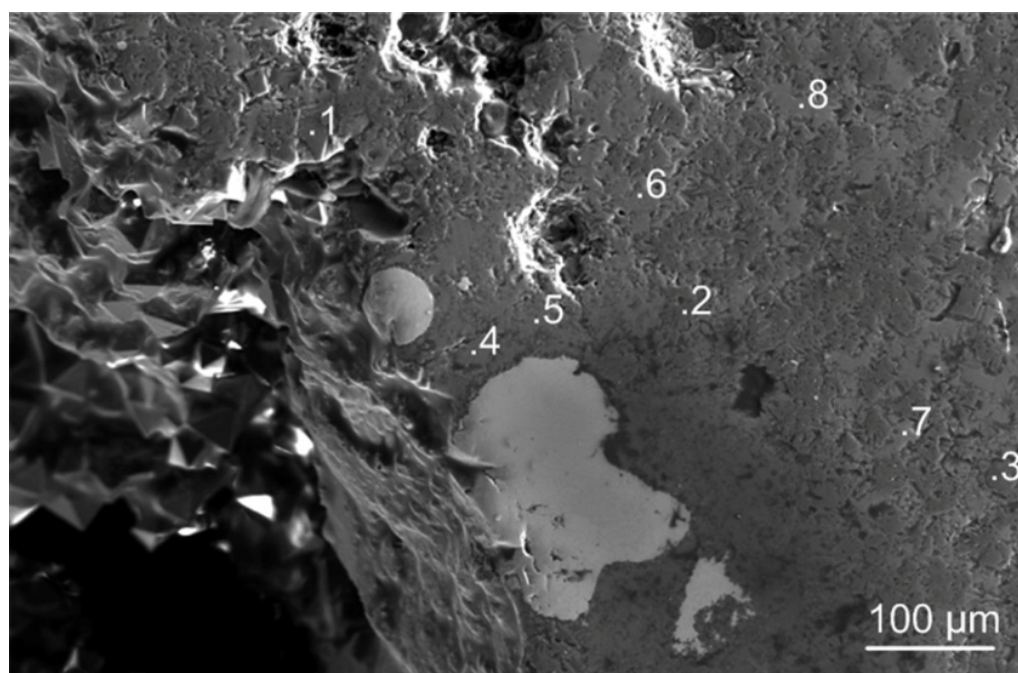


Figure 3. BSE image of slag area at the slag–weld metal interface: MP1 slag sample. (See Table 5 for the analyses of the numbered phases in Figure 3).

Table 5. SEM analyses of marked phase positions in Figure 3 (mass%).

Position	%Al	%Mg	%Ca	%F	%Si	%Ti	%Mn	%Fe	%Na	%K	%O	Phase
1	27.1	15.1	0.5	0	1.1	6.3	3.2	0.2	0	0	46.6	Spinel
2	28.9	15.1	0	0.3	0	2.4	1.8	0.5	0	0	51.0	Spinel
3	27.8	14.9	0.2	0	0.3	4.5	2.6	0.3	0	0	49.5	Spinel
4	1.0	9.8	25.2	14.4	11.8	1.4	6.3	0.2	1.5	0	28.4	Glass
5	0.7	10.2	23.6	16.6	9.9	1.2	4.8	0.1	1.7	0	31.2	Glass
6	0.5	9.2	26.5	20.8	9.2	1.8	4.1	0.1	1.6	0	26.2	Glass
7	0.9	8.7	25.0	23.0	9.5	2.1	4.6	0	1.4	0	24.8	Glass
8	0.5	9.5	25.2	22.3	10.0	1.9	4.4	0.1	1.7	0	24.4	Glass
Bulk Slag	16.7	14.0	8.0	5.3	7.1	3.2	3.5	3.1	1.2	0.2	37.6	

Figure 4a shows the BSE image of a smaller area in the MP1 slag, and Figure 4b shows EDX mapping of this area. It is clear from the data displayed in Figure 4b that the larger angular crystals are the spinel crystals embedded in a matrix of Al-Mg-Ca-F-Si-Ti-Mn-Fe-K-Na-O oxy-fluoride glass phase from which Al-Mg-Si-Ti-Mn-O containing small phase areas appear to be exsolved upon cooling. Interestingly, Ti is distributed across all phases, in agreement with the phase analyses in Table 5. However, it is seen from the EDX maps that the distribution of Ti is not uniform, because Ti appears to be present in higher concentrations at the outer edges of the large spinel crystals, metal areas and at points inside the exsolved Al-Mg-Si-Ti-Mn-O phase areas. The spinel crystals are typically 40 μm in cross-sectional dimension.

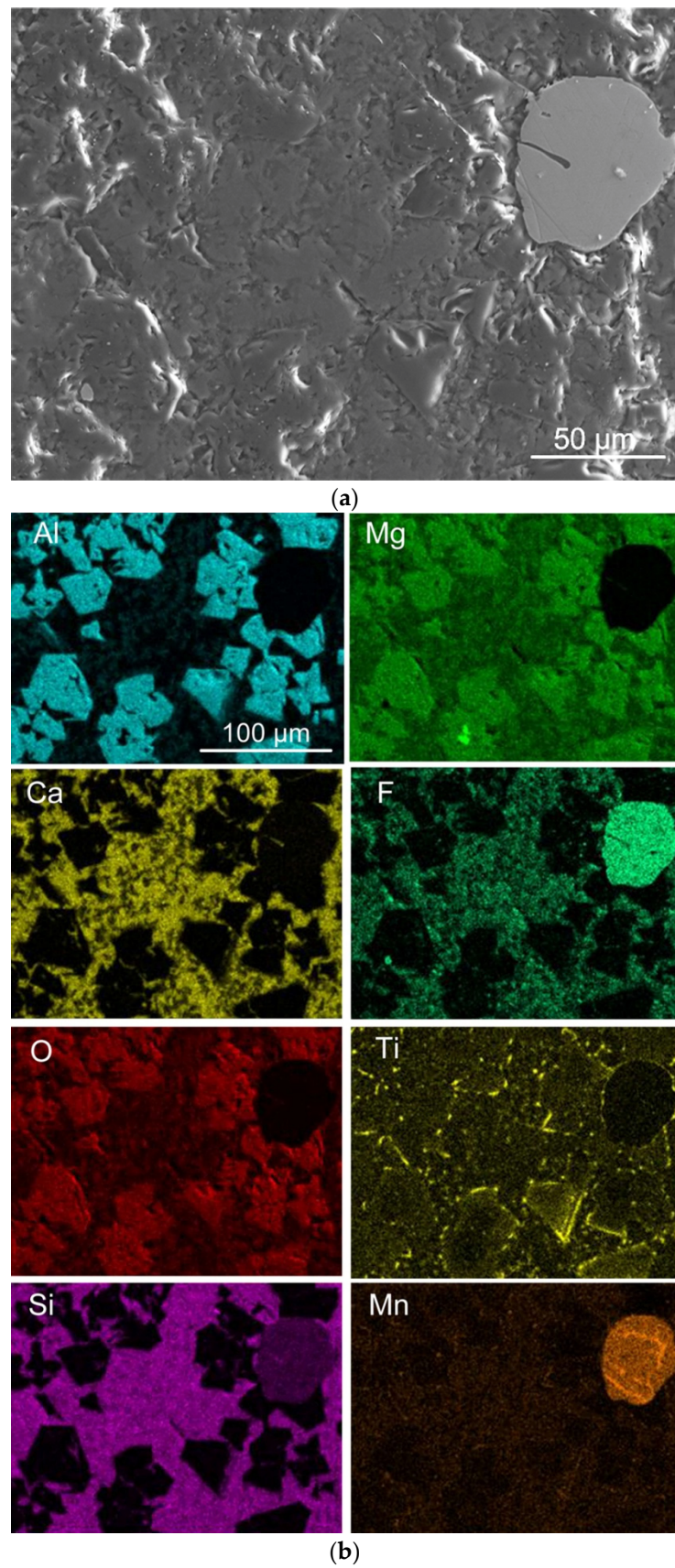


Figure 4. (a) BSE image of a smaller area in the MP1 slag sample. (b) EDX map of area in Figure 4a: MP1 slag sample.

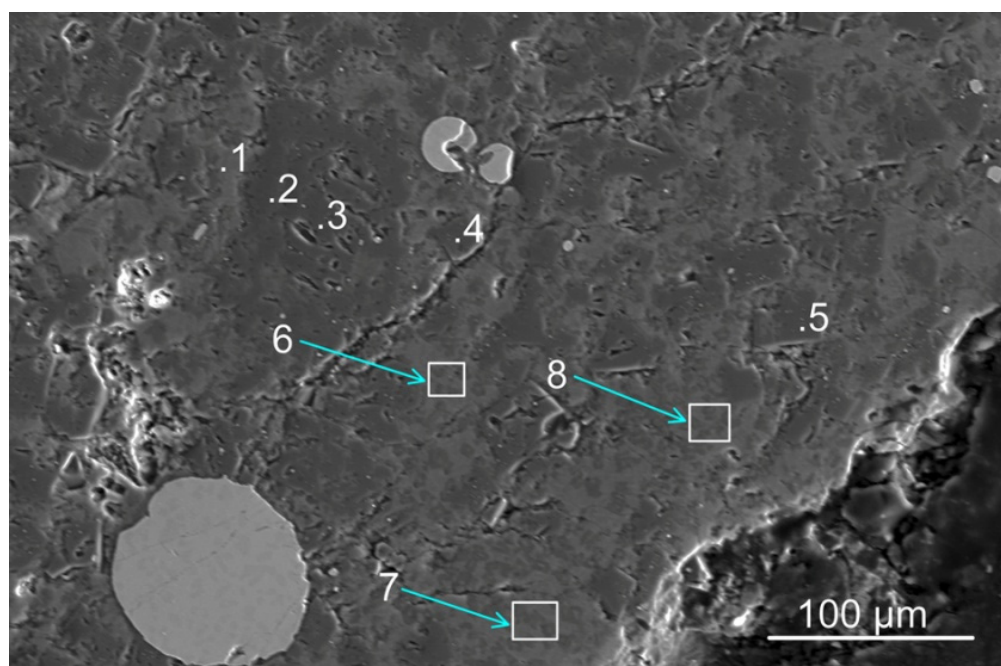


Figure 5. BSE image of slag area at the slag–weld metal interface: MP3 slag sample. (See Table 6 for the analyses of the numbered phases in Figure 5).

Table 6. SEM analyses of marked phase positions in Figure 5 (mass%).

Position	%Al	%Mg	%Ca	%F	%Si	%Ti	%Mn	%Fe	%Na	%K	%O	Phase
1	1.3	6.4	27.1	12.7	8.8	0.7	3.6	0	1.5	0	38.0	Glass
2	33.0	11.7	0.5	0	0.2	0.6	2.4	0.2	0	0	51.2	Spinel
3	45.4	0	0.1	0	0	0.1	0.1	0.7	0	0	53.6	Alumina
4	29.9	14.8	0.2	0	0.2	1.8	1.4	0.5	0	0	51.2	Spinel
5	25.4	13.8	6.5	0	1.7	1.3	2.0	0.1	0.2	0	49.1	Spinel
6	4.0	8.7	15.6	13.9	9.6	1.4	2.3	0	1.6	0.2	42.6	Glass
7	4.7	9.5	14.9	12.4	10.2	1.5	2.3	0	1.7	0.2	42.6	Glass
8	3.6	8.5	16.3	12.8	9.1	1.4	2.4	0	1.5	0.2	44.2	Glass
Bulk Slag	18.4	11.0	6.3	4.2	5.5	8.7	2.9	3.5	0.9	0.1	38.6	

Figure 5 shows the phase assemblage of an area in the MP3 slag. The phases in the MP3 slag are similar to those in the MP1 slag, consisting of spinel crystals set in the oxy-fluoride glass matrix phase. The phases in Figure 5 contain less Ti than the phases in Figure 3, although Ti is incorporated into both the oxy-fluoride glass matrix and spinel phases in slags MP1 and MP3. It is possible that some of the Ti analysed in the bulk slag composition in Table 3 represent metallic Ti. Comparison of the phase chemistries at positions 2 and 3 in Figure 5 and Table 6 indicates the modification of pure Al_2O_3 to spinel (MgAl_2O_4).

Figure 6a shows the BSE image of a smaller area in Figure 5, and Figure 6b shows EDX mapping of this area. The element distribution in Figure 6b corresponds to that in Figure 4b as angular spinel crystals embedded in the Al-Mg-Ca-F-Si-Ti-Mn-Fe-K-Na-O oxy-fluoride glass phase matrix, with small phase areas of Al-Mg-Si-Ti-Mn-O phase exsolved upon cooling. Titanium is distributed across all phases, with higher concentrations at the edges of the large spinel crystals and as points inside the exsolved Al-Mg-Si-Ti-Mn-O phase areas. The spinel crystals are typically of 25 μm in cross-sectional dimension.

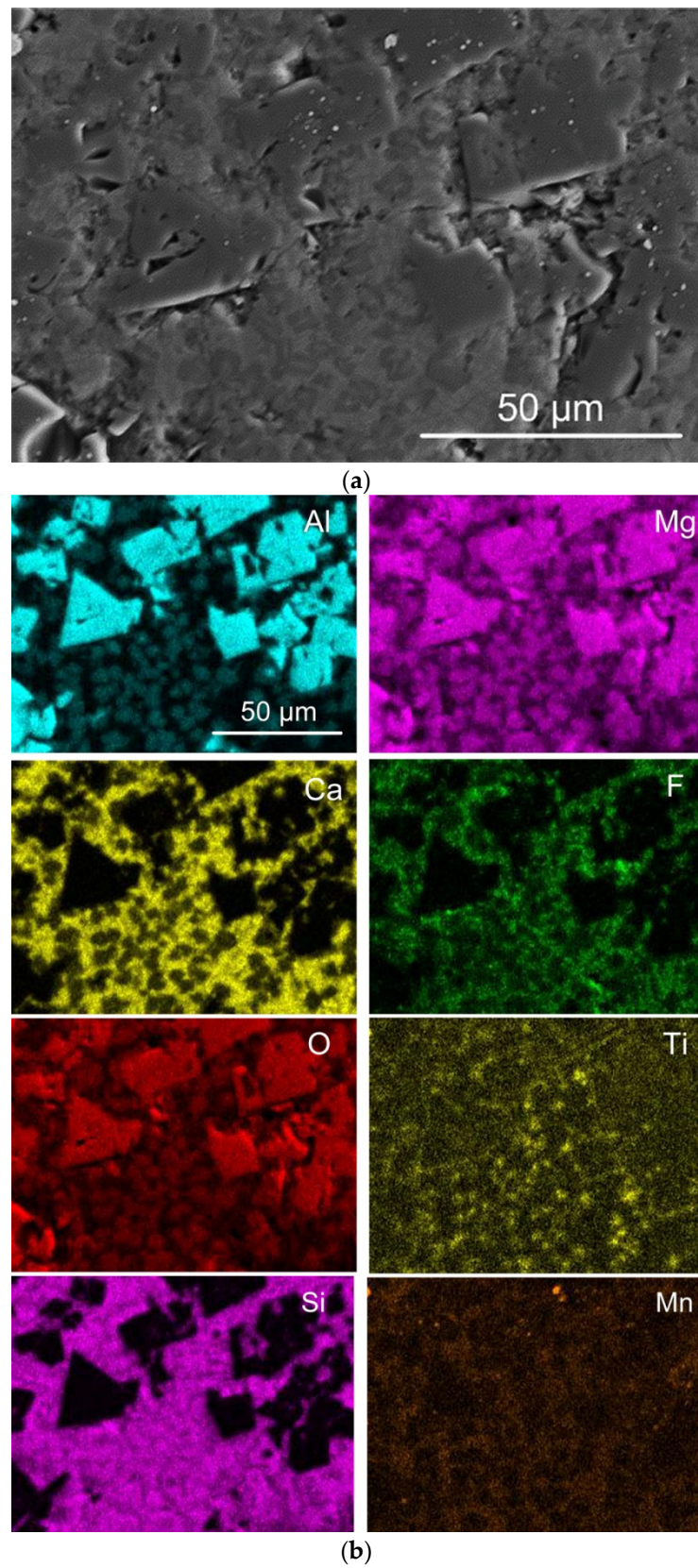


Figure 6. (a) BSE image of a smaller area in MP3 slag sample. (b) EDX map of slag area in Figure 6a: MP3 slag.

4. Discussion

The solid crystalline phases present in the polished sections displayed in Figures 2–6 may have formed as cooling phases as the post-weld slag cooled down from the high welding temperatures close to 2000 °C in the weld pool to room temperature [7,8]. This possibility was investigated by calculating the phase solidification curves for each slag composition in Table 3, using the Equilib module in FactSage 7.3 thermochemical software, and selecting the FToxid database [40,41]. Although there are no multi-component phase diagrams of the system of interest in this study, the FactSage thermochemical software calculation outputs for the CaO-SiO₂-MgO-Al₂O₃-CaF₂ system were confirmed to be accurate compared with some equilibrated slag samples in a previous study [44]. Therefore, the FactSage calculations in this study are used with confidence as the basis of the expanded multi-component system relevant to our study. In addition, there are a few published studies available on the phase chemistry and physico-chemical properties of fluxes in the system of Al₂O₃-MgO-CaF₂-Na₂O-K₂O-Fe₂O₃ [9,10,45]. These studies confirmed that the MgO and Al₂O₃ in the flux reacted to form spinel upon heating of the flux, even at temperatures as low as 700–800 °C, and more easily at 1200 °C to 1500 °C. Spinel phase formation occurred even when the flux glass phase was only partially molten at 1200 °C [9]. The authors confirmed that the lighter spinel phase floated from the bulk slag. Furthermore, the authors point out that the differences in thermal expansion coefficients of the spinel phase and the liquid slag phase may be used to induce micro-stresses in the slag to ensure good separation between the slag and the underlying metal [9]. This is an important design aspect in the development of welding fluxes because it ensures good bead shape, surface finish and high welding productivity [17].

The solidification curves in Figure 7a–d are in general agreement with the reported high-temperature-phase chemistry in this flux system, namely, the presence of a liquid slag phase and solid spinel crystallites [9,10]. The solidification curve calculations predict that the flux mixture was completely liquid at the weld pool temperature reported in the literature, 2000 °C [7,8]. Upon cooling, spinel precipitated as the primary solidification phase. Due to the increased alumina content in the modified MP1 and MP3 slags, the percentage spinel phase is increased to double that of the BC slag at 1400 °C. Clearly the increased alumina content in the MP1 and MP3 slags would significantly increase the two-phase slag viscosity, compared with the unaltered BC slag viscosity [9,45]. As indicated before, due to the exponential increase in slag viscosity with increased solid phase proportion, even slight increases in the proportion of spinel phase in the slag result in a drastic increase in slag viscosity [10]. Slag viscosity is double that of the CaF₂ matrix phase with every 10 mass% increase in solid phase [46]. Figure 7d shows the liquid glass curves from Figure 7a–c for easier comparisons. The curves illustrate that although the slag liquidus temperatures are similar at 1682 °C, 1730 °C and 1670 °C, the precipitation phase formation sequence sets these slags apart. For example, at 1400 °C the BC slag contains 25% spinel phase, compared with 38–39% spinel in the MP1 and MP3 slag. Increased spinel content in the MP1 and MP3 slags is due to the higher quantity of Al₂O₃ present in the MP1 and MP3 slags, in combination with fewer glass matrix formation compounds of SiO₂ and MnO from aluminothermic reduction of the slag. Furthermore, it appears that at the lower temperatures close to 1000 °C, the higher TiO₂ in MP3 slag somewhat compensates for the increased spinel phase formation due to higher %Al₂O₃ and lower %SiO₂ and %CaF₂ contained, as compared with the MP1 slag.

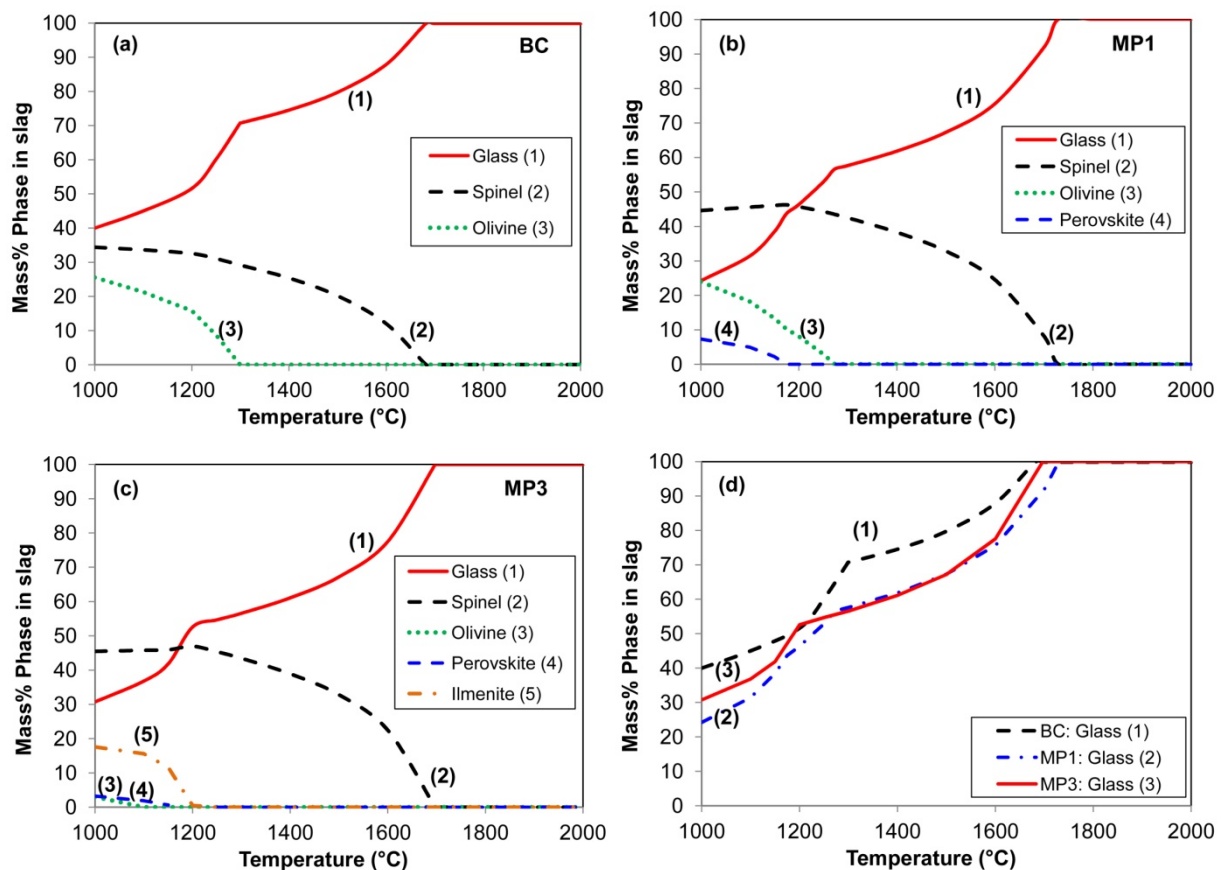


Figure 7. (a–d) Solidification curves for post-weld slags as calculated in FactSage 7.3 [40,41].

Another aspect in the investigation of slag detachability is the difference in solidification temperatures of the slag and the weld metal. Table 7 summarises the weld metal alloy solidus temperatures and the spinel proportions in each slag at 1400 °C and at the weld pool solidus temperature, as calculated in FactSage 7.3. The value of 1400 °C is considered with reference to the flux design guideline that the slag should be melting at 50 °C below the solidus temperature of carbon steel [6]. However, MP1 and MP3 weld metals have lower solidus temperatures than carbon steel resulting in increased spinel content in the MP1 and MP3 slags at the weld metal solidus temperatures, of approximately 40% spinel phase compared with only 23% spinel phase in the BC slag. Therefore, it is conceivable that the MP1 and MP3 weld bead surface morphology is solidified as rough surfaces due to the high spinel content as the cause of high viscosity slags at the weld pool–slag interface. The result is mechanical fixation of the slag to the rough weld bead surface, identified previously for different welding conditions [18].

Table 7. Comparison of weld pool solidus temperatures and slag spinel content.

Sample	Weld Pool Solidus Temperature (°C)	Slag Spinel Content at 1400 °C (Mass%)	Slag Spinel Content at Weld Pool Solidus Temperature (Mass%)
BC	1457	25	23
MP1	1363	38	40
MP3	1311	39	43

As pointed out above, the spinel phase grows from oxide slag according to the parabolic rate law at higher temperatures, in the order of 1400 °C [10,47]. Figure 8 shows the growth rate relationship reported in the literature applied here to calculate the time

required for a spinel crystal to grow to a specific size at different temperatures. At 1700 °C, close to the liquidus temperatures of slags BC, MP1 and MP3, the rate equation predicts that a 10 µm spinel crystal can crystallise and grow from the molten glass phase in 2.0 s and a 20 µm crystal in 7.9 s. The BC weld metal solidification time was calculated to be about four seconds, using the weld ripple lag distance and travel speed [32,33]. In comparison, the typical spinel crystal sizes observed in the BSE images of Figures 2, 4 and 6 are 20 µm, 40 µm and 25 µm in the BC, MP1 and MP3 slags, respectively. These observations are in agreement with the formation of the larger spinel crystals observed in MP1 slag (40 µm) from the enhanced process whereby Al₂O₃ is formed in aluminothermic reduction, and not only from spinel formation from the matrix glass phase.

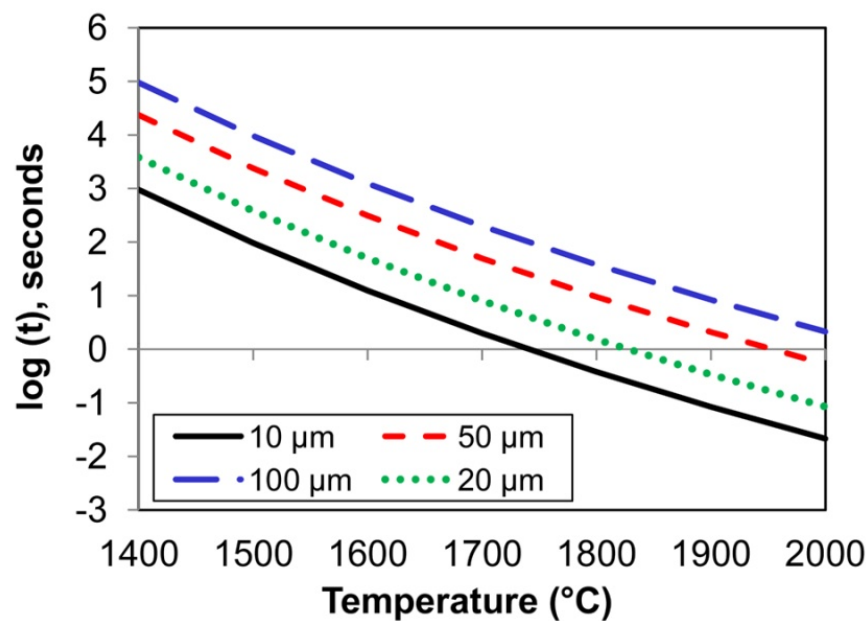


Figure 8. Estimated spinel growth rates calculated from the growth equation in reference [47].

The relative phase changes in the slags are further analysed in the following pseudo-ternary phase diagrams to chart possible improvements in flux formulations to compensate for the increased Al₂O₃ and decreased SiO₂ and MnO in the slag, when using aluminium as deoxidiser element in SAW. The pseudo-ternary phase diagrams in the CaF₂-SiO₂-Al₂O₃-MgO-TiO₂-FeO system were calculated in the Phase Diagram module of FactSage 7.3, by selecting the FToxid database. These diagrams are not as precise in their thermochemical phase boundaries as the curves in Figure 7, because here only the approximate compositions in terms of the major composition compounds are considered. However, in Figure 7, the precise compositions as shown in Table 3 are used as inputs to the calculations. Figure 9a–c displays the pseudo-ternary diagrams at 1400 °C for the fixed %SiO₂, %TiO₂ and %FeO for each post-weld slag composition, and each post-weld slag composition is indicated as a filled marker. The %CaO and %MnO were not specified because these low-percentage compounds may be easily incorporated into the oxy-fluoride matrix phase, as displayed in Figures 4 and 6. Figure 9a–c shows that the 1400 °C liquidus boundary is moved little with changes in %SiO₂ and %TiO₂. The phase field of interest, the (liquid + spinel) phase field, is somewhat enlarged as the (liquid + olivine + spinel) phase field shrinks with increased %TiO₂.

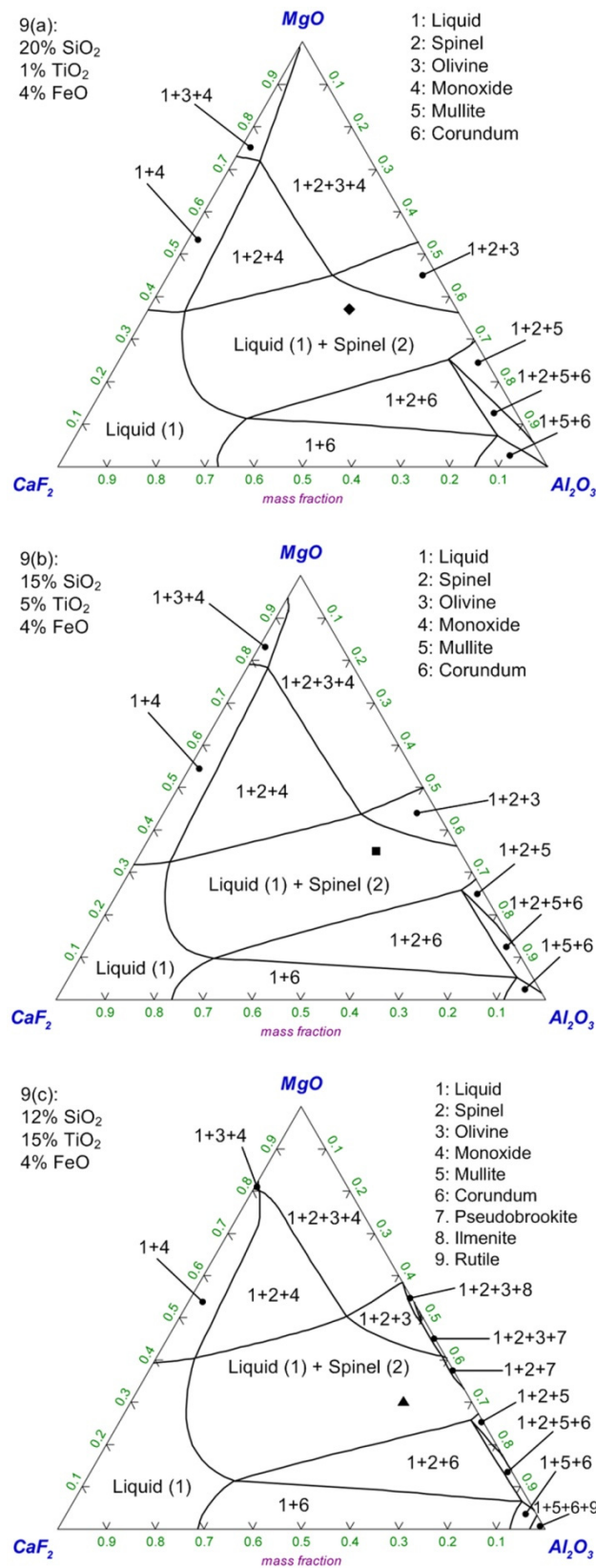


Figure 9. (a–c) CaF₂-SiO₂-Al₂O₃-MgO-TiO₂-FeO pseudo-ternary phase diagrams for 1400 °C, as calculated in FactSage 7.3 [40,41].

By increasing the %CaF₂ in the starting flux, the slag composition may be adjusted to accommodate the additional spinel from the aluminothermic reduction process. This is

illustrated in Figure 10 in which the BC flux composition was adjusted to attain approximately 20% spinel at 1250 °C. These adjustments in %CaF₂ should sufficiently compensate for the increase in percentage Al₂O₃ in the slag from aluminothermic reduction, to prevent viscosity and slag detachability problems caused by excessive spinel formation at the lowered alloy steel solidus temperatures.

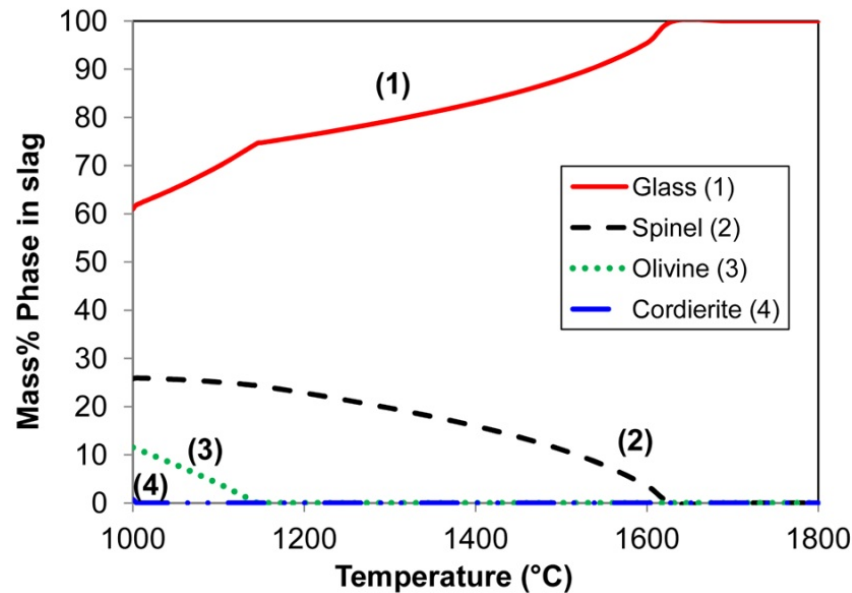


Figure 10. Solidification curve for the adjusted flux chemistry composition (30% CaF₂–23% SiO₂–23% Al₂O₃–23% MgO), as calculated in FactSage 7.3 [40,41].

Therefore, the flux should be formulated to manage the slag phase proportions of matrix oxy-fluoride glass phase to spinel crystals. Increasing the proportion of matrix oxy-fluoride glass phase in the slag will ensure a fluid slag at lower temperatures to improve slag detachability. As highlighted in previous studies, the flux CaF₂ content should be increased to increase the proportion glass matrix phase in the slag, but also to reduce the size and increase the dispersion of spinel crystals formed upon solidification of the slag [8,43].

5. Conclusions

1. The aluminate basic flux was modified to increased %Al₂O₃ and %TiO₂ and decreased %SiO₂ and %MnO due to aluminothermic reduction;
2. Titanium was incorporated in the two-phase post-weld slag, in both the oxy-fluoride glass matrix and in the spinel phase;
3. Increased quantities of spinel crystals were formed in the modified slag from added alumina, resulting in increased slag viscosity;
4. The combination of increased flux viscosity due to spinel formation and lowered weld pool solidus temperatures caused a rough bead surface morphology which, in turn, caused mechanical fixation of the slag to the weld bead surface;
5. Increased %CaF₂ in the flux formulation should compensate sufficiently for the increased spinel formation from Al₂O₃ added into the slag due to aluminothermic reduction, and thus prevent viscosity and slag detachability problems caused by excessive spinel formation.

Author Contributions: F.D.B. conceptualised the study; F.D.B. and T.C. performed the experiments, interpreted the data, and prepared the manuscript. All authors have read and agreed to the published version of the manuscript.

Funding: This research was funded in part by the National Research Foundation of South Africa, grant number BRIC171211293679.

Data Availability Statement: The data sets presented in this study are available upon request from the corresponding author.

Conflicts of Interest: The authors declare no conflict of interest. The funders had no role in the design of the study; in the collection, analyses, or interpretation of data; in the writing of the manuscript, or in the decision to publish the results.

References

1. Sengupta, V.; Havrylov, D.; Mendex, P.F. Physical phenomena in the weld zone of submerged arc welding—A Review. *Weld. J.* **2019**, *98*, 283–313.
2. Gött, G.; Gericke, A.; Henkel, K.-M.; Uhrlandt, D. Optical and spectroscopic study of a submerged arc welding cavern. *Weld. J.* **2016**, *95*, 491–499.
3. Linnert, G.E. *Welding Metallurgy-Carbon and Alloy Steels, Volume I-Fundamentals*, 4th ed.; American Welding Society (AWS): Miami, FL, USA, 1994; pp. 706–758.
4. O'Brien, A. *Welding Handbook. Volume 2—Welding Processes, Part 1*, 9th ed.; American Welding Society (AWS): Miami, FL, USA, 1994; pp. 256–282.
5. Palm, J.H. How fluxes determine the metallurgical properties of Submerged Arc Welds. *Weld. J.* **1972**, *51*, 358–360.
6. Singh, B.; Khan, Z.A.; Siddiquee, A.N. Effect of flux composition on element transfer during Submerged Arc Welding (SAW): A literature review. *Int. J. Curr. Res.* **2013**, *5*, 4181–4186.
7. Chai, C.S.; Eagar, T.W. Slag-metal equilibrium during submerged arc welding. *Metall. Trans. B* **1981**, *12*, 539–547. [[CrossRef](#)]
8. Mitra, U.; Eagar, T.W. Slag-metal reactions during welding: Part I. Evaluation and reassessment of existing theories. *Metall. Trans. B* **1991**, *22*, 65–71. [[CrossRef](#)]
9. Sokolsky, V.E.; Roik, O.S.; Davidenko, A.O.; Kazimirov, V.P.; Lisnyak, V.V.; Galinich, V.I.; Goncharov, I.A. The phase evolution at high-temperature treatment of the oxide-fluoride ceramic flux. *Res. J. Chem. Sci.* **2014**, *4*, 71–77.
10. Davidenko, A.O.; Sokolsky, V.E.; Lisnyak, V.V.; Roik, O.S.; Goncharov, I.A.; Galinich, V.I. The effect of spinel formation in the ceramic welding fluxes on the properties of molten slag. *Res. J. Chem. Sci.* **2015**, *5*, 23–31.
11. Golovko, V.V.; Potapov, N.N. Special features of agglomerated (ceramic) fluxes in welding. *Weld. Int.* **2011**, *25*, 889–893. [[CrossRef](#)]
12. Mills, K.C. Structure and properties of slags used in the continuous casting of steel: Part 1 Conventional Mould Powders. *ISIJ Int.* **2016**, *56*, 1–13. [[CrossRef](#)]
13. Sharma, L.; Kumar, J.; Chhibber, R. Experimental investigation on high temperature wettability and structural behaviour of SAW fluxes using MgO-TiO₂-SiO₂ and Al₂O₃-MgO-SiO₂ flux system. *Ceram. Int.* **2020**, *46*, 5649–5657. [[CrossRef](#)]
14. Zhang, Y.; Coetsee, T.; Yang, H.; Zhao, T.; Wang, C. Structural roles of TiO₂ in CaF₂-SiO₂-CaO-TiO₂ submerged arc welding fluxes. *Metall. Trans. B* **2020**, *51*, 1947–1952. [[CrossRef](#)]
15. Wang, A.; Sohn, I. Review on the high-temperature thermophysical properties of continuous casting mold fluxes for highly alloyed steels. *ISIJ Int.* **2020**, *60*, 2705–2716. [[CrossRef](#)]
16. Shi, C. Deoxidation of electroslag remelting (ESR)—A Review. *ISIJ Int.* **2020**, *60*, 1083–1096. [[CrossRef](#)]
17. Moravetsky, S.I. Detachability of slag crust in arc welding (Review) Part 1: Mechanism of chemical adhesion of slag crust to weld metal. *Paton Weld. J.* **2011**, *1*, 28–31.
18. Moravetsky, S.I. Detachability of slag crust in arc welding (Review) Part 2: Character of the effect of main factors on detachability of slag crust. *Paton Weld. J.* **2011**, *2*, 20–23.
19. Mitra, U.; Eagar, T.W. Slag metal reactions during submerged arc welding of alloy steels. *Metall. Trans. B* **1984**, *15*, 217–227. [[CrossRef](#)]
20. Kohno, R.; Takamo, T.; Mori, N.; Nagano, K. New fluxes of improved weld metal toughness for HSLA steels. *Weld. J.* **1982**, *61*, 373–380.
21. Sham, K.; Lui, S. Flux-coating development for SMAW consumable electrode of high-nickel alloys. *Weld. J.* **2014**, *93*, 271–281.
22. Mitra, U.; Eagar, T.W. Slag-metal reactions during welding: Part II. Theory. *Metall. Trans. B* **1991**, *22*, 73–81. [[CrossRef](#)]
23. Mitra, U.; Eagar, T.W. Slag-metal reactions during welding: Part III. Verification of the Theory. *Metall. Trans. B* **1991**, *22*, 83–100. [[CrossRef](#)]
24. Polar, A.; Indacochea, J.E.; Blander, M. Electrochemically generated oxygen contamination in submerged arc welding. *Weld. J.* **1990**, *69*, 68–74.
25. Lau, T.; Weatherly, G.C.; Mc Lean, A. The sources of oxygen and nitrogen contamination in submerged arc welding using CaO-Al₂O₃ based fluxes. *Weld. J.* **1985**, *64*, 343–347.
26. Chai, C.S.; Eagar, T.W. Slag metal reactions in binary CaF₂-metal oxide welding fluxes. *Weld. J.* **1982**, *61*, 229–232.

27. Eagar, T.W. Sources of weld metal oxygen contamination during submerged arc welding. *Weld. J.* **1978**, *57*, 76–80.
28. Du Plessis, J.; Du Toit, M.; Pistorius, P.C. Control of diffusible weld metal hydrogen through flux chemistry modification. *Weld. J.* **2007**, *86*, 273–280.
29. Park, J.-Y.; Chang, W.-S.; Sohn, I. Effect of MnO to hydrogen dissolution in CaF₂-CaO-SiO₂ based welding type fluxes. *Sci. Technol. Weld. Join.* **2012**, *17*, 134–140. [[CrossRef](#)]
30. Tuliani, S.S.; Boniszewski, T.; Eaton, N.F. Notch toughness of commercial submerged arc weld metal. *Weld. Met. Fabr.* **1969**, *37*, 327–339.
31. Klucken, A.O.; Grong, Ø. Mechanisms of inclusion formation in Al-Ti-Si-Mn deoxidized steel weld metals. *Metall. Trans. B* **1989**, *20*, 1335–1349. [[CrossRef](#)]
32. Coetsee, T.; Mostert, R.J.; Pistorius, P.G.H.; Pistorius, P.C. The effect of flux chemistry on element transfer in Submerged Arc Welding: Application of thermochemical modelling. *Mater. Res. Technol.* **2021**, *11*, 2021–2036. [[CrossRef](#)]
33. Zhang, J.; Coetsee, T.; Wang, C. Element transfer behaviors of fused CaF₂-SiO₂ fluxes subject to high heat input submerged arc welding. *Metall. Trans. B* **2020**, *51*, 16–21. [[CrossRef](#)]
34. Zhang, J.; Coetsee, T.; Dong, H.; Wang, C. Element transfer behaviors of fused CaF₂-SiO₂-MnO fluxes under high heat input submerged arc welding. *Metall. Trans. B* **2020**, *51*, 885–890. [[CrossRef](#)]
35. Zhang, J.; Coetsee, T.; Dong, H.; Wang, C. Element Transfer Behaviors of fused CaF₂-TiO₂ Fluxes in EH36 Shipbuilding steel during high heat input Submerged Arc Welding. *Metall. Trans. B* **2020**, *51*, 1953–1957. [[CrossRef](#)]
36. Coetsee, T.; De Bruin, F.J. Improved titanium transfer in Submerged Arc Welding of carbon steel through aluminium addition. *Miner. Process. Extr. Metall. Rev.* **2021**, 1–4. [[CrossRef](#)]
37. Coetsee, T.; De Bruin, F.J. Reactions at the molten flux-weld pool interface in submerged arc welding. *High Temp. Mater. Process.* **2021**, *40*, 421–427. [[CrossRef](#)]
38. Coetsee, T.; De Bruin, F. Application of Copper as Stabiliser in Aluminium Assisted Transfer of Titanium in Submerged Arc Welding of Carbon Steel. *Processes* **2021**, *9*, 1763. [[CrossRef](#)]
39. Coetsee, T.; De Bruin, F. Chemical Interaction of Cr-Al-Cu Metal Powders in Aluminum-Assisted Transfer of Chromium in Submerged Arc Welding of Carbon Steel. *Processes* **2022**, *10*, 296. [[CrossRef](#)]
40. Bale, B.R.; Chartrand, P.; Degterov, S.A.; Errikson, G. FactSage thermochemical software and databases. *Calphad* **2002**, *26*, 189–228. [[CrossRef](#)]
41. FactSage.com. Available online: <https://www.factsage.com/> (accessed on 5 May 2022).
42. Coetsee, T. Phase chemistry of Submerged Arc Welding (SAW) fluoride based slags. *Mater. Res. Technol.* **2020**, *9*, 9766–9776. [[CrossRef](#)]
43. Sokolsky, V.E.; Roik, O.S.; Davidenko, A.O.; Kazimirov, V.P.; Lisnyak, V.V.; Galinich, V.I.; Goncharov, I.A. X-ray diffraction and SEM/EDX studies on technological evolution of the oxide-fluoride ceramic flux for Submerged Arc-Surfacing. *J. Min. Metall. Sect. B* **2012**, *48*, 101–113. [[CrossRef](#)]
44. Park, J.H. Solidification structure of CaO-SiO₂-MgO-Al₂O₃ (-CaF₂) systems and computational phase equilibria: Crystallization of MgAl₂O₄ spinel. *Calphad* **2007**, *31*, 428–437. [[CrossRef](#)]
45. Goncharov, I.A.; Sokolsky, V.E.; Davidenko, A.O.; Galinich, V.I.; Mischenko, D.D. Formation of spinel in melt of the MgO-Al₂O₃-SiO₂-CaF₂ system agglomerated welding flux and its effect on viscosity of slag. *Paton Weld. J.* **2012**, *12*, 18–25.
46. Turkdogan, E.T. *Physicochemical Properties of Molten Slags and Glasses*; The Metals Society: London, UK, 1983; pp. 11–17.
47. Nightingale, S.A.; Monaghan, B.J. Kinetics of Spinel formation and growth during dissolution of MgO in CaO-Al₂O₃-SiO₂ slag. *Metall. Trans. B* **2008**, *39*, 643–648. [[CrossRef](#)]